IOP Publishing Journal of Geophysics and Engineering
J. Geophys. Eng. 14 (2017) 520–532 (13pp) https://doi.org/10.1088/1742-2140/aa5e67

Seismic acoustic impedance inversion with multi-parameter regularization

Shu Li[1,2,3] **and Zhenming Peng**[1,2,4]

[1] School of Optoelectronic Information, University of Electronic Science and Technology of China, Chengdu 610054, People's Republic of China
[2] Center for Information Geoscience, University of Electronic Science and Technology of China, Chengdu 610054, People's Republic of China
[3] School of Information Science and Engineering, Jishou University, Jishou 416000, People's Republic of China

E-mail: dawning2008@qq.com and zmpeng@uestc.edu.cn

Received 19 May 2016, revised 8 January 2017
Accepted for publication 6 February 2017
Published 28 March 2017

Abstract

Most acoustic impedance sparse inversion methods include two parts: reflectivity inversion and extraction of acoustic impedance from reflectivity. This being the case, the acoustic impedance is easily affected by reflectivity and the value of acoustic impedance at time $t = 0$, thus may become inaccurate. In this paper, we propose a seismic acoustic impedance inversion method with multi-parameter regularization. In our method, the acoustic impedance is calculated directly from objective functions to ensure the stability and accuracy of results. In addition, the total variation regularization, L1 norm constraint, and initial model constraint are used to make the inversion results better accordant with *a priori* geological information. Moreover, we use multi-trace inversion to reflect the spatial and temporal correlation of the data. Since the objective function contains several different types of regularization term, we have developed an algorithm based on split Bregman iteration to calculate it. The inversion results of theoretical model and field data show that the proposed method has high inversion precision, strong anti-noise ability and good performance on stratigraphy delineation.

Keywords: L1 norm, total variation, impedance inversion, regularization

(Some figures may appear in colour only in the online journal)

1. Introduction

Seismic acoustic impedance (AI) is a rock property that is intimately related to lithology, porosity, pore fill, and other factors (Latimer *et al* 2000). Obtaining AI from seismic data is one of the central goals of reflection seismology (Walker and Ulrych 1983, Ghosh 2000). To achieve this goal, scholars have put forward many AI inversion methods. They are very useful for quantitative interpretation of seismic data (Mabrouk 2010, Hao *et al* 2014). Therefore, AI inversion is always the research hotspot of exploration seismology. The conventional AI inversion methods, such as Band-limited Inversion (Lindseth 1979), Generalized Linear Inversion (Cooke and Schneider 1983), Stochastic Sparse-spike Inversion (Velis 2006, 2008) are based on an L2 norm optimization approach with Tikhonov-type regularization. These methods are easily affected by the noise in seismic data, and this may lead to incorrect inversion results (Liu *et al* 2015). In addition, these methods also cause vertical interfaces to appear too smooth, making it difficult to distinguish formation boundaries (Zhang *et al* 2013).

While the seismic inversion methods based on L2 norm regularization were flourishing, the L1 norm regularization method was also becoming more and more popular in seismic inversion. It has been widely used in the fields of seismic deconvolution (Taylor *et al* 1979, Levy and Fullagar 1981, Santosa and Symes 1986), inversion (Oldenburg *et al* 1983, Bube and Langan 1997, Loris *et al* 2007), data reconstruction (Zwartjes and Gisolf 2007), and multiple removal (Guitton and Verschuur 2004), etc. In this paper, we focus on its application in AI inversion. In recent years, the new progress

[4] Author to whom any correspondence should be addressed.

in this area has mainly been as follows. Wang (2010) proposed an L1 norm constrained regularization model for AI inversion, and developed a nonmonotone gradient descent method to solve the regularization problem. Zhang *et al* (2014) proposed a seismic inversion method based on L1 norm misfit function with total variation (TV) regularization. This method is appropriate to solving the inverse problem when outliers exist in the seismic data and discontinuities such as layer interfaces need to be clearly delineated. Liu *et al* (2015) proposed an L1 norm regularized inversion method which has strong anti-noise ability. These L1 norm regularization AI inversion methods are generally implemented by two sequential inversion steps (called Two-step AI inversion based on L1 norm regularization): first, the L1 norm is used to impose the sparse constraint on the reflectivity, by solving the L1 norm optimization problem to obtain the sparse reflectivity. The second step is to invert the reflectivity for AI using a recursion formula.

However, there are some defects in these methods. In the first step, the reflectivity obtained may be inaccurate due to the band-limit of seismic data and the noise (Berteussen and Ursin 1983, Cooke and Schneider 1983, Hendrick and Hearn 1993). In the second step, AI is obtained from $\mathbf{I}(t) = \mathbf{I}(t_0)\exp\left[2\int_{t_0}^{t}\mathbf{R}(\eta)\mathrm{d}\eta\right]$ (Zhang *et al* 2014), where $\mathbf{I}(t)$ is the AI at time $= t$, $\mathbf{R}$ is the reflectivity, and $\mathbf{I}(t_0)$ is the AI at time $t = 0$. We can find that the result of AI inversion depends on the AI at time $t = 0$ and the result of the reflectivity obtained from the first step. If $\mathbf{I}(t_0)$ or $\mathbf{R}$ is inaccurate, the result of the AI will not be accurate. Actually, the AI at the time $t = 0$ is usually very difficult to find precisely. Furthermore, there is a difference between the reflectivity obtained from the first step and the true reflectivity. Meanwhile, the AI is obtained from the reflectivity by integrating, which can result in the error of the reflectivity at the present time being accumulated to the AI at the subsequent times. The AI sparse inversion method proposed in this paper can solve this problem. In our method, the logarithm of AI is the optimization target, and we have no need to know the AI at time $t = 0$. Due to the excellent work of Goldstein and Osher (2009), we can use the split Bregman iteration algorithm to solve this kind of optimization problem. Using the proposed method we can obtain the AI and reflectivity simultaneously.

Most conventional inversion methods are trace-by-trace operations, and thus do not allow spatial regularization of the AI map. Trace-by-trace inversion results are easily affected by noise, leading to a noisy AI section and so masking important geologic features (Hamid and Pidlisecky 2015). Therefore, some scholars put forward the multi-trace AI inversion method. Gholami (2015) proposed nonlinear multichannel AI inversion based on TV regularization. He first used the robust and automatic multichannel blind deconvolution algorithm to extract the reflectivity section from the data. Then he solved the nonlinear AI problem by inverting the generated reflectivity model to a regularized AI model. Yuan *et al* (2015) presented the simultaneous multi-trace AI inversion with transform-domain sparsity promotion. The authors found that the proposed method contributes to stabilizing the inversion, reducing the influence of high-wavenumber noise on the inverted result, and exploring spatial continuities of structures. Hamid and Pidlisecky (2015) put forward the multi-trace AI inversion with lateral constraints. The inversion results produced well-defined horizontal boundaries, while suppressing noise.

TV regularization is suitable for extracting discontinuities or sudden changes in AI, such as strong faults or salt bodies (Zhang *et al* 2014). Therefore, Zhang *et al* applied TV regularization to AI inversion. Gholami (2015) applied the TV regularization to nonlinear multichannel AI inversion to obtain blocky AI structures. In order to outline the abrupt changes in AI and obtain blocky AI structures, TV regularization is used in our method. Furthermore, considering the band-limited nature of seismic data, we add an initial model constraint as a regularization term to ensure the inversion result contains low frequency information and reduce non-uniqueness of the inversion.

TV regularization, L1 norm regularization, initial model constraints and multi-trace inversion have different effects on the AI inversion. These regularization constraints have been used in existing AI inversion methods, but there is no method using all these regularization constraints simultaneously. There is no doubt that more *a priori* constraints used in inverse problems lead to better inversion results. For this reason, this article presents the multi-trace AI sparse inversion method with the TV regularization, L1 norm regularization and initial model constraint. Due to these regularization constraints, the objective function contains several different types of regularization term. We adopt the split Bregman iterative algorithm to decouple it into several simple formulae for calculation.

The main innovations of this paper are as follows: (1) The AI is obtained directly from the objective function rather than the reflectivity. (2) TV regularization, L1 norm regularization, initial model constraint and multi-trace inversion are all used in the inversion process to improve the inversion quality. (3) An algorithm is developed to solve seismic inversion problems containing several different types of regularization term.

2. Methodology

2.1. Forward model

A convolution model is often used as the forward model in the seismic inversion. A single seismic trace can be expressed as

$$\mathbf{s}(\mathbf{t}) = \mathbf{w}(\mathbf{t}) \otimes \mathbf{r}(\mathbf{t}) + \mathbf{n}(\mathbf{t}) \tag{1}$$

where $\mathbf{s}(\mathbf{t})$ is the seismic trace, $\mathbf{w}(\mathbf{t})$ is a band-limited wavelet assumed to be stationary, $\mathbf{t}$ represents the time series, the symbol '$\otimes$' indicates the convolution operation, $\mathbf{r}(\mathbf{t})$ represents the reflectivity, and $\mathbf{n}(\mathbf{t})$ represents the noise.

In the AI inversion, if the AI $\mathbf{i}(\mathbf{t})$ can be expressed as a continuous function of time $\mathbf{t}$, then the reflectivity $\mathbf{r}(\mathbf{t})$ can be

written as (Russell 1988).

$$\mathbf{r(t)} = \frac{\mathbf{di(t)}}{\mathbf{dt}} \frac{1}{2\mathbf{i(t)}}. \tag{2}$$

Equation (2) can be written as

$$\mathbf{r(t)} = \frac{1}{2} \frac{\mathbf{d}\,\ln(\mathbf{i(t)})}{\mathbf{dt}}. \tag{3}$$

Yilmaz (2001) pointed out that for a strong reflecting layer a representative reflectivity is about 0.2. When the reflectivity is less than 0.3, (3) can be discretized as (Walker and Ulrych 1983)

$$\begin{bmatrix} \mathbf{r}(1) \\ \mathbf{r}(2) \\ \vdots \\ \mathbf{r}(m-1) \end{bmatrix} = \frac{1}{2} \begin{bmatrix} -1 & 1 & & & \\ & -1 & 1 & & \\ & & \ddots & \ddots & \\ & & & -1 & 1 \end{bmatrix} \begin{bmatrix} \ln(\mathbf{i}(1)) \\ \ln(\mathbf{i}(2)) \\ \vdots \\ \ln(\mathbf{i}(m)) \end{bmatrix}. \tag{4}$$

Let **D** be the form of equation (5)

$$\mathbf{D} = \frac{1}{2} \begin{bmatrix} -1 & 1 & & & \\ & -1 & 1 & & \\ & & \ddots & \ddots & \\ & & & -1 & 1 \end{bmatrix} \tag{5}$$

then (4) in matrix form as

$$\mathbf{r} = \mathbf{D}\ \mathbf{l} \tag{6}$$

where $\mathbf{r} = [r(1)\ \ r(2)\ \ \cdots\ \ r(m-1)]^T$ and $\mathbf{l} = [\ln(i(1))\ \ln(i(2))\ \cdots\ \ln(i(m))]^T$ are the 1D reflectivity and the logarithm of AI respectively. T denotes the transpose. m is the number of sampling point of AI.

The 2D seismic convolution model can be expressed as

$$\mathbf{S} = \mathbf{W}^*\mathbf{R} + \mathbf{N} \tag{7}$$

where **S** is the 2D seismic section, **W** is the wavelet matrix, **R** is the 2D reflectivity matrix, the symbol '*' indicates matrix multiplication, and **N** represents the 2D noise matrix. If the length of wavelet and reflectivity are p and q respectively, then **W** can be written as

$$\mathbf{W} = \begin{bmatrix} w_1 & & & \\ w_2 & w_1 & & \\ \vdots & w_2 & \ddots & \\ w_p & \vdots & \ddots & w_1 \\ & w_p & \ddots & w_2 \\ & & \ddots & \vdots \\ & & & w_p \end{bmatrix}_{(p+q-1)*q}. \tag{8}$$

If we extend the reflectivity and AI in (6) to the 2D case, by (6) and (7), the relation between the 2D seismic section and the AI can be written as

$$\mathbf{S} = \mathbf{WR} + \mathbf{N} = \mathbf{WDL} + \mathbf{N} \tag{9}$$

where **L** represents the 2D logarithm of AI section. We can find that the reflectivity is the link between the seismic record and the AI.

2.2. The proposed method

In order to overcome the shortcomings of the two-step AI inversion based on L1 norm regularization, we propose an AI sparse inversion method. In our objective function, the logarithm of AI is used as the parameter that needs to be inverted. Considering that the reflectivity is sparse in the time domain, the L1 norm regularization is imposed on it. We use multi-trace inversion to reflect the spatial and temporal correlation of the data. In this case, the seismic data, reflectivity and the logarithm of AI are reorganized as column vectors. Considering the L1 norm regularization and multi-trace inversion, the objective function can be given by

$$J(\tilde{\mathbf{L}}, \mathbf{R}) = \min_{\tilde{\mathbf{L}}} \frac{\mu}{2} \|G\tilde{\mathbf{L}} - \tilde{\mathbf{S}}\|_2^2 + \|\mathbf{R}\|_1 \quad \text{s.t. } \mathbf{R} = \hat{\mathbf{D}}\tilde{\mathbf{L}} \tag{10}$$

where $\tilde{\mathbf{L}} = \mathrm{vec}(\ln(\mathbf{I}(t)))$ and $\tilde{\mathbf{S}} = \mathrm{vec}(\mathbf{S})$ are column vectors, $\tilde{\mathbf{L}}$ is obtained by aligning the logarithm of AI section, $\tilde{\mathbf{S}}$ is generated by arranging seismic section, $\hat{\mathbf{D}} = \mathrm{kron}(\mathbf{E}, \mathbf{D})$ is a block diagonal matrix which is the Kronecker product of identity matrix **E** and the matrix **D** defined in (5), **R** represents the reflectivity which is a column vector, μ is the regularization parameter of the fidelity term, $\mathbf{G} = \mathrm{kron}(\mathbf{E}, \mathbf{WD})$is a block diagonal matrix which is the Kronecker product of identity matrix **E** and **WD**. **WD** is the product of matrix **W** and **D** defined in (8) and (5).

A penalty function is used to convert (10) to be an unconstrained optimization problem for simplification. Then, (10) is changed to be (11) with a regularization parameter

$$J(\tilde{\mathbf{L}}, \mathbf{R}) = \min_{\tilde{\mathbf{L}}} \frac{\mu}{2} \|\mathbf{G}\tilde{\mathbf{L}} - \tilde{\mathbf{S}}\|_2^2 + \|\mathbf{R}\|_1 + \frac{\gamma}{2} \|\mathbf{R} - \hat{\mathbf{D}}\tilde{\mathbf{L}}\|_2^2 \tag{11}$$

In order to outline the abrupt part of the AI clearly and obtain blocky AI structures, a TV regularization term is added to the objective function, that is

$$J(\tilde{\mathbf{L}}, \mathbf{R}) = \min_{\tilde{\mathbf{L}}} \frac{\mu}{2} \|\mathbf{G}\tilde{\mathbf{L}} - \tilde{\mathbf{S}}\|_2^2 + \|\mathbf{R}\|_1 + \frac{\gamma}{2} \|\mathbf{R} - \hat{\mathbf{D}}\tilde{\mathbf{L}}\|_2^2 + \sum_{i,j} \sqrt{(\nabla_x \tilde{\mathbf{L}})_{i,j}^2 + (\nabla_y \tilde{\mathbf{L}})_{i,j}^2} \tag{12}$$

where $\sum_{i,j} \sqrt{(\nabla_x \tilde{\mathbf{L}})_{i,j}^2 + (\nabla_y \tilde{\mathbf{L}})_{i,j}^2}$ is the TV of $\tilde{\mathbf{L}}$. For convenience, we use the short-hand notation

$$\|(d_x, d_y)\|_2 = \sum_{i,j} \sqrt{(\nabla_x \tilde{\mathbf{L}})_{i,j}^2 + (\nabla_y \tilde{\mathbf{L}})_{i,j}^2} \tag{13}$$

where $d_x = \nabla_x \tilde{\mathbf{L}}$, $d_y = \nabla_y \tilde{\mathbf{L}}$ are the difference of $\tilde{\mathbf{L}}$ in x and y directions respectively. Then, (12) can be written as the constrained optimization problem

$$\begin{aligned} J(\tilde{\mathbf{L}}, \mathbf{R}) = \min_{\tilde{\mathbf{L}}} & \frac{\mu}{2} \|\mathbf{G}\tilde{\mathbf{L}} - \tilde{\mathbf{S}}\|_2^2 + \|\mathbf{R}\|_1 \\ & + \frac{\gamma}{2} \|\mathbf{R} - \hat{\mathbf{D}}\tilde{\mathbf{L}}\|_2^2 + \|(d_x, d_y)\|_2 \\ s.t.\ \ & d_x = \nabla_x \tilde{\mathbf{L}},\ d_y = \nabla_y \tilde{\mathbf{L}}. \end{aligned} \tag{14}$$

We can convert (14) to be an unconstrained optimization problem by the Lagrangian method

$$J(\tilde{\mathbf{L}}, \mathbf{R}) = \min_{\tilde{\mathbf{L}}} \frac{\mu}{2} \|\mathbf{G}\tilde{\mathbf{L}} - \tilde{\mathbf{S}}\|_2^2 + \|\mathbf{R}\|_1 + \|(d_x, d_y)\|_2 + \frac{\gamma}{2} \|\mathbf{R} - \hat{\mathbf{D}}\tilde{\mathbf{L}}\|_2^2 + \frac{\lambda}{2} \|d_x - \nabla_x \tilde{\mathbf{L}}\|_2^2 + \frac{\lambda}{2} \|d_y - \nabla_y \tilde{\mathbf{L}}\|_2^2 \quad (15)$$

where γ is a regularization parameter.

The initial model constraint is added to the objective function to incorporate the corresponding low frequency content to the AI and reduce the non-uniqueness of inversion. Finally, the objective function is written as:

$$J(\tilde{\mathbf{L}}, \mathbf{R}) = \min_{\tilde{\mathbf{L}}} \frac{\mu}{2} \|\mathbf{G}\tilde{\mathbf{L}} - \tilde{\mathbf{S}}\|_2^2 + \|\mathbf{R}\|_1 + \|(d_x, d_y)\|_2 + \frac{\gamma}{2} \|\mathbf{R} - \hat{\mathbf{D}}\tilde{\mathbf{L}}\|_2^2 + \frac{\lambda}{2} \|d_x - \nabla_x \tilde{\mathbf{L}}\|_2^2 + \frac{\lambda}{2} \|d_y - \nabla_y \tilde{\mathbf{L}}\|_2^2 + \frac{\alpha}{2} \|\tilde{\mathbf{L}} - \mathbf{L}'\|_2^2 \quad (16)$$

where α is the regularization parameter of the initial model constraint term, $\mathbf{L}'$ is a column vector obtained by rearranging the logarithm of the initial AI model section or volume.

It can be seen that multiple regularization constraints are added to the objective function, which becomes a complicated formula with L1 norm, TV norm and L2 norm. According to the work of Goldstein and Osher (2009), we can use the split Bregman iteration algorithm to solve this kind of multi-regularized optimization problem (Kong and Peng 2015). Using the split Bregman iteration algorithm, an objective function with different regularization constraints can be 'decoupled' into several simpler sub-problems.

In order to illustrate the solving process of the multi-regularized optimization problem proposed in this paper, the key step of the split Bregman iteration algorithm will be introduced briefly. For an unconstrained optimization problem (17), $\Phi(u)$ and $H(u)$ are convex functions, $|\bullet|$ represents the L1 norm and λ is the regularization parameter of the fidelity term

$$\min_{d,u} |d| + H(u) + \frac{\lambda}{2} \|d - \Phi(u)\|_2^2. \quad (17)$$

To solve (17), the auxiliary variable b is taken to decouple the L2 norm regularization term by split Bregman iteration. Then, (17) is split to (18), (19), where k represents the kth iteration

$$(u^{k+1}, d^{k+1}) = \min_{u,d} |d| + H(u) + \frac{\lambda}{2} \|d - \Phi(u) - b^k\|_2^2 \quad (18)$$

$$b^{k+1} = b^k + (\Phi(u^{k+1}) - d^{k+1}). \quad (19)$$

Equation (18) can be further split into (20) and (21), which are the optimization problems about u and d, respectively

$$u^{k+1} = \min_u H(u) + \frac{\lambda}{2} \|d^k - \Phi(u) - b^k\|_2^2 \quad (20)$$

$$d^{k+1} = \min_d |d| + \frac{\lambda}{2} \|d - \Phi(u) - b^k\|_2^2. \quad (21)$$

In our method, the objective function contains multiple regularization terms. To solve it, the auxiliary variables b_x, b_y and b_R are taken to the objective function. According to the split Bregman iteration algorithm, (16) can be written as the following form

$$J(\tilde{\mathbf{L}}, \mathbf{R}) = \min_{\tilde{\mathbf{L}}} \frac{\mu}{2} \|\mathbf{G}\tilde{\mathbf{L}} - \tilde{\mathbf{S}}\|_2^2 + \|\mathbf{R}\|_1 + \|(d_x, d_y)\|_2 + \frac{\gamma}{2} \|\mathbf{R} - \hat{\mathbf{D}}\tilde{\mathbf{L}} - b_R\|_2^2 + \frac{\lambda}{2} \|d_x - \nabla_x \tilde{\mathbf{L}} - b_x\|_2^2 + \frac{\lambda}{2} \|d_y - \nabla_y \tilde{\mathbf{L}} - b_y\|_2^2 + \frac{\alpha}{2} \|\tilde{\mathbf{L}} - \mathbf{L}'\|_2^2. \quad (22)$$

The objective function (22) can be decoupled into the simpler sub-problems (23)–(25) to solve (Goldstein and Osher 2009)

$$\tilde{\mathbf{L}}^{k+1} = \min_{\tilde{\mathbf{L}}} \frac{\mu}{2} \|\mathbf{G}\tilde{\mathbf{L}} - \tilde{\mathbf{S}}\|_2^2 + \frac{\gamma}{2} \|\mathbf{R}^k - \hat{\mathbf{D}}\tilde{\mathbf{L}} - b_R^k\|_2^2 + \frac{\lambda}{2} \|d_x^k - \nabla_x \tilde{\mathbf{L}} - b_x^k\|_2^2 + \frac{\lambda}{2} \|d_y^k - \nabla_y \tilde{\mathbf{L}} - b_y^k\|_2^2 + \frac{\alpha}{2} \|\tilde{\mathbf{L}} - \mathbf{L}'\|_2^2 \quad (23)$$

$$(d_x^{k+1}, d_y^{k+1}) = \min_{d_x, d_y} \|(d_x, d_y)\|_2 + \frac{\lambda}{2} \|d_x^k - \nabla_x \tilde{\mathbf{L}} - b_x^k\|_2^2 + \frac{\lambda}{2} \|d_y^k - \nabla_y \tilde{\mathbf{L}} - b_y^k\|_2^2 \quad (24)$$

$$\mathbf{R}^{k+1} = \text{shrink}\left(\hat{\mathbf{D}}\tilde{\mathbf{L}}^{k+1} + b_R^k, \frac{1}{\gamma}\right). \quad (25)$$

The function shrink( ) in (25) is a shrinkage operator defined as

$$\text{shrink}(x, \gamma) = \frac{x}{|x|} * \max(|x| - \gamma, 0) \quad (26)$$

Equation (24) can be further split into (27) and (28)

$$d_x^{k+1} = \max\left(h^{k+1} - \frac{1}{\lambda}, 0\right) \frac{\nabla_x \tilde{\mathbf{L}}^{k+1} + b_x^k}{h^{k+1}} \quad (27)$$

$$d_y^{k+1} = \max\left(h^{k+1} - \frac{1}{\lambda}, 0\right) \frac{\nabla_y \tilde{\mathbf{L}}^{k+1} + b_y^k}{h^{k+1}} \quad (28)$$

where

$$h^{k+1} = \sqrt{|\nabla_x \tilde{\mathbf{L}}^{k+1} + b_x^k|^2 + |\nabla_y \tilde{\mathbf{L}}^{k+1} + b_y^k|^2}. \quad (29)$$

For more details about the split Bregman iteration algorithm, the reader can refer to the work of Goldstein and Osher (2009).

There are several regularization parameters in the objective function (22). Although it is unrealistic to give a set of parameters that can be applied to any conditions, fully understanding the meaning of each parameter can help us to determine the values of these parameters, and obtain good inversion results. The parameter μ is the weight of the fidelity term. It determines the fitting between the synthetic traces obtained from the inversion result and the original seismic traces. The higher the quality of seismic data is, the greater the value of μ can be set. However, the value of the fidelity term is usually much larger than other terms. Only when μ is a small value can the other regularization terms be effective. Moreover, noise often exists in seismic data, and we do not need a perfect fit. Therefore, we should set μ to be a small value. The parameter γ determines the fitting of the reflectivity $\mathbf{R}$ and $\hat{\mathbf{D}}\tilde{\mathbf{L}}$ in (23). The greater γ is, the better $\mathbf{R}$ and $\hat{\mathbf{D}}\tilde{\mathbf{L}}$ will fit. The fitting between the difference of L in x/y directions and d_x/d_y depends on λ. The larger λ is, the better they will fit. The parameter α is the weight of the initial model constraint. It determines the fitting degree of the inversion result and initial model. When the noise in the seismic data is larger, α is increased; otherwise, it is decreased. If α is too large, the inversion result will be biased towards the initial model, and other regularization parameters will not work. Conversely, when α is too small, the initial model constraint does not work. To choose a set of parameters, we can do quality control at a theoretical model or at the well locations. The specific process is to adjust the regularization parameters and select a set of parameters which make the inversion result fit the true model data or true well log data best.

Algorithm 1 illustrates the technical details of the method proposed in this paper.

Algorithm 1. AI inversion with multi-parameter regularization

Input: μ, γ, λ, α, *tol*

1. Initialize: $k = 0$, $d_x^0 = d_y^0 = b_x^0 = b_y^0 = b_R^0 = R^0 = \mathbf{0}$, $\mathbf{L}'$
2. While $\|\tilde{\mathbf{L}}^k - \tilde{\mathbf{L}}^{k-1}\|_2 / \|\tilde{\mathbf{L}}^k\|_2 > tol$
3. $$\tilde{\mathbf{L}}^{k+1} = \min_{\tilde{\mathbf{L}}} \frac{\mu}{2}\|G\tilde{\mathbf{L}} - \tilde{\mathbf{S}}\|_2^2 + \frac{\gamma}{2}\|\mathbf{R}^k - \hat{\mathbf{D}}\tilde{\mathbf{L}} - b_R^k\|_2^2 + \frac{\lambda}{2}\|d_x^k - \nabla_x\tilde{\mathbf{L}} - b_x^k\|_2^2 + \frac{\lambda}{2}\|d_y^k - \nabla_y\tilde{\mathbf{L}} - b_y^k\|_2^2 + \frac{\alpha}{2}\|\tilde{\mathbf{L}} - \mathbf{L}'\|_2^2$$
4. $$h^{k+1} = \sqrt{|\nabla_x\tilde{\mathbf{L}}^{k+1} + b_x^k|^2 + |\nabla_y\tilde{\mathbf{L}}^{k+1} + b_y^k|^2}$$
5. $$d_x^{k+1} = \max\left(h^{k+1} - \frac{1}{\lambda}, 0\right)\frac{\nabla_x\tilde{\mathbf{L}}^{k+1} + b_x^k}{h^{k+1}}$$
6. $$d_y^{k+1} = \max\left(h^{k+1} - \frac{1}{\lambda}, 0\right)\frac{\nabla_y\tilde{\mathbf{L}}^{k+1} + b_y^k}{h^{k+1}}$$
7. $$\mathbf{R}^{k+1} = shrink\left(\hat{\mathbf{D}}\tilde{\mathbf{L}}^{k+1} + b_R^k, \frac{1}{\gamma}\right)$$
8. $$b_x^{k+1} = b_x^k + (\nabla_x\tilde{\mathbf{L}}^{k+1} - d_x^{k+1})$$
9. $$b_y^{k+1} = b_y^k + (\nabla_y\tilde{\mathbf{L}}^{k+1} - d_y^{k+1})$$
10. $$b_R^{k+1} = b_R^k + (\hat{\mathbf{D}}\tilde{\mathbf{L}}^{k+1} - \mathbf{R}^{k+1})$$
11. $k = k + 1$
12. End
13. $\mathbf{I} = reshape(\exp(\tilde{\mathbf{L}}^k))$

In algorithm 1, step 3 is the process of calculating the logarithm of the AI, to find the optimal value of $\tilde{\mathbf{L}}$. Note that (23) is the sum of the L2 norm terms, Setting the derivative of equation (23) with respect to $\tilde{\mathbf{L}}$ to 0 gives rise to the following equation

$$\begin{aligned}(\mu\mathbf{G}^T\mathbf{G} + \lambda\nabla_x^T\nabla_x + \lambda\nabla_y^T\nabla_y + \gamma\hat{\mathbf{D}}^T\hat{\mathbf{D}} + \alpha\mathbf{E})\tilde{\mathbf{L}} \\ = \mu\mathbf{G}^T\tilde{\mathbf{S}} + \lambda\nabla_x^T(d_x - b_x) + \lambda\nabla_y^T(d_y - b_y) \\ + \gamma\hat{\mathbf{D}}^T(\mathbf{R} - b_R) + \alpha\mathbf{L}'\end{aligned} \tag{30}$$

where $\mathbf{E}$ is an identity matrix; let:

$$\begin{aligned}\mathbf{A} &= \mu\mathbf{G}^T\mathbf{G} + \lambda\nabla_x^T\nabla_x + \lambda\nabla_y^T\nabla_y + \gamma\hat{\mathbf{D}}^T\hat{\mathbf{D}} + \alpha\mathbf{E} \\ \mathbf{B} &= \mu\mathbf{G}^T\tilde{\mathbf{S}} + \lambda\nabla_x^T(d_x - b_x) + \lambda\nabla_y^T(d_y - b_y) \\ &\quad + \gamma\hat{\mathbf{D}}^T(\mathbf{R} - b_R) + \alpha\mathbf{L}'.\end{aligned}$$

Equation (30) can be written as $A\tilde{\mathbf{L}} = \mathbf{B}$, which can be solved efficiently by the conjugate gradient method.

Steps 5 and 6 are the generalized shrinkage formula used to obtain the optimal value of d_x and d_y, respectively. Step 7 is the standard shrinkage formula to get the optimal value of $\mathbf{R}$. When the relative change of the L2 norm of $\tilde{\mathbf{L}}$ is less than the threshold *tol*, the 'while' loop will be stopped, and then the optimal value of $\tilde{\mathbf{L}}$ is obtained. Step 13 calculates the exponent of $\tilde{\mathbf{L}}$ firstly, and then through the process of reshape() $\tilde{\mathbf{L}}$ is converted to an AI section or volume.

3. Numerical examples

We will now test the efficiency of the proposed method using Marmousi2 model data (Martin *et al* 2006) and field data. We also compare the inversion result with those obtained from another two methods. The first such method is based on L1 norm regularization, multi-trace inversion and initial model constraint (it is denoted as method 1 and does not include TV regularization). The second method is based on TV regularization, multi-trace inversion and initial model constraint (it is denoted as method 2 and does not include L1 norm regularization).

3.1. Marmousi2 model

In this article, we take part of the Marmousi2 model for testing of our method, method 1 and method 2. The true AI model data is a 1140 × 1940 AI section (there are 1140 sampling points in the depth direction and 1940 traces in the distance direction), which is shown in figure 1(a). Sampling interval in the depth direction is 2.5 m, and in the distance direction is 3.75 m. The parameters are set as follows: $\mu = 1 \times 10^{-4}$, $\gamma = 10$, $\lambda = 100$, $\alpha = 1$ and tol $= 1 \times 10^{-5}$. Since method 1 does not have TV regularization, it does not use the parameter λ. Similarly, method 2 does not use the parameter γ.

Before the AI model inversion experiment, we have to produce synthetic seismic data, which can be obtained by equation (1). Firstly, we use equation (4) to calculate the reflectivity of the true AI model, which is shown in figure 1(b)

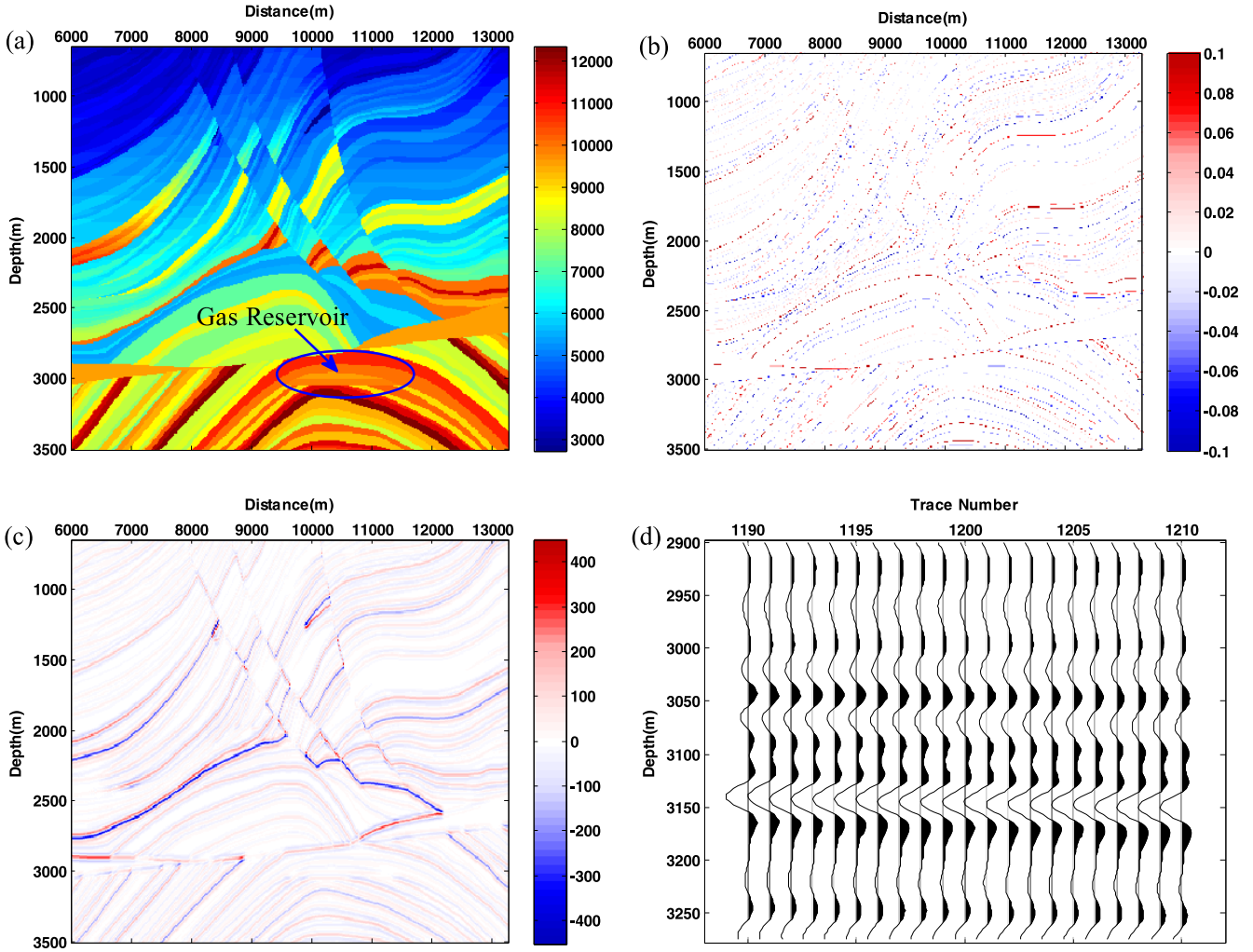

Figure 1. (a) True AI model, (b) reflectivity section of true AI model, (c) synthetic seismic data and (d) part of seismic data taken from synthetic seismic data.

(we change the color scale to [−0.1 0.1] to better emphasize details). Secondly, through calculating the convolution of a Ricker wavelet with dominant frequency 40 Hz and the reflectivity, a synthetic seismic section without noise is obtained, which is shown in figure 1(c). Figure 1(d) shows part of seismic data taken from figure 1(c). Finally, 20% Gaussian random noise (the energy ratio of noise to signal is 20%) is added to the noise-free synthetic seismic section to generate a noisy synthetic seismic section, which is shown in figure 2(a). The noisy synthetic seismic section is used as the original seismic record. Figure 2(b) shows the initial AI model, which is obtained from the true AI model by Gauss low-pass filtering.

Because of the large area of the seismic section, we divide it into several blocks to speed up the calculation speed. The size of each block is 140 × 140. Each time we invert one of the blocks. Then the inversion result of each block is spliced into the final result. We do some experiments on the Marmousi2 model by using method 1, method 2 and our method. Figures 3(a)–(c) show the inversion results of method 1, method 2 and our method respectively. It can be seen that, compared with method 1, our method and method 2 describe the formation structure more clearly. In figure 1, the position of the arrow is a gas reservoir, which is circled by an ellipse. Our method and method 2 reveal the gas reservoir more clearly than method 1. Furthermore, the inversion error of our method and method 2 is also less than method 1. Comparing to figure 1, we can find that there is a serious error in figure 3(a). However, inversion results in figures 3(b) and (c) are much closer to the ground truth, and the error is smaller.

In order to compare the inversion results in detail, figure 3(d) shows the inversion result of a part of the data from trace 1200. Trace 1200 is a seismic trace through the gas reservoir. Because there are too many sampling points in each trace, in order to compare the inversion results of these three kinds of method clearly, we take out the inversion results and true AI model between 2525 m and 3275 m. The red solid line, blue dashed line, black dash-dotted line and black solid line represent, respectively, the true AI model, inversion result of method 1, inversion result of method 2 and inversion result of our method. It can be found that the inversion result of our method is the closest to the true model, method 2 take the second place, and method 1 has the largest deviation.

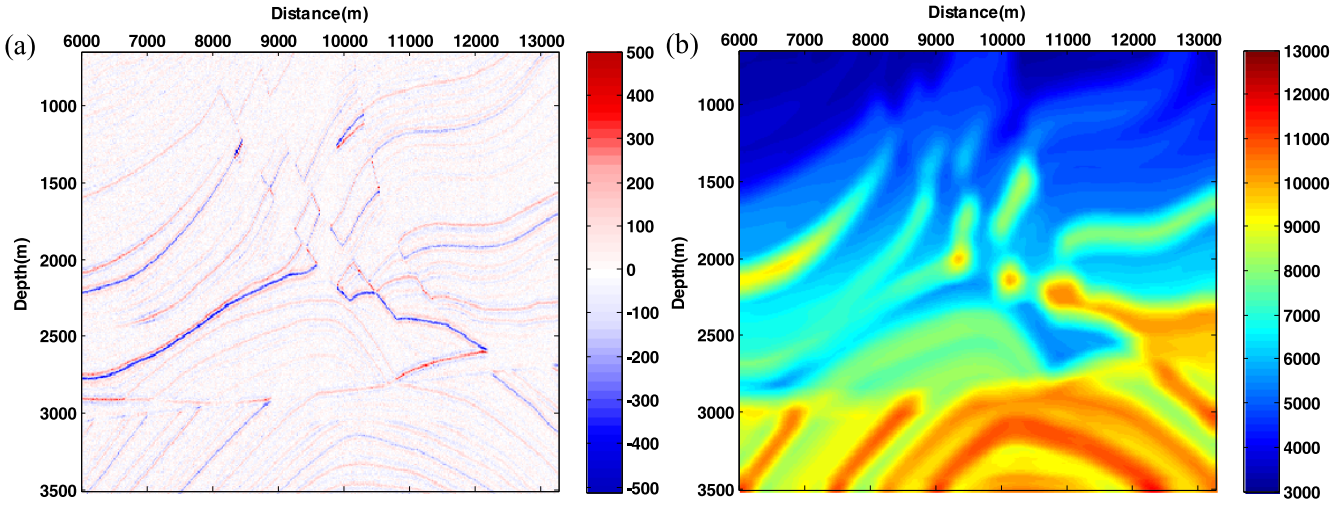

Figure 2. (a) Noisy synthetic seismic section and (b) initial AI model.

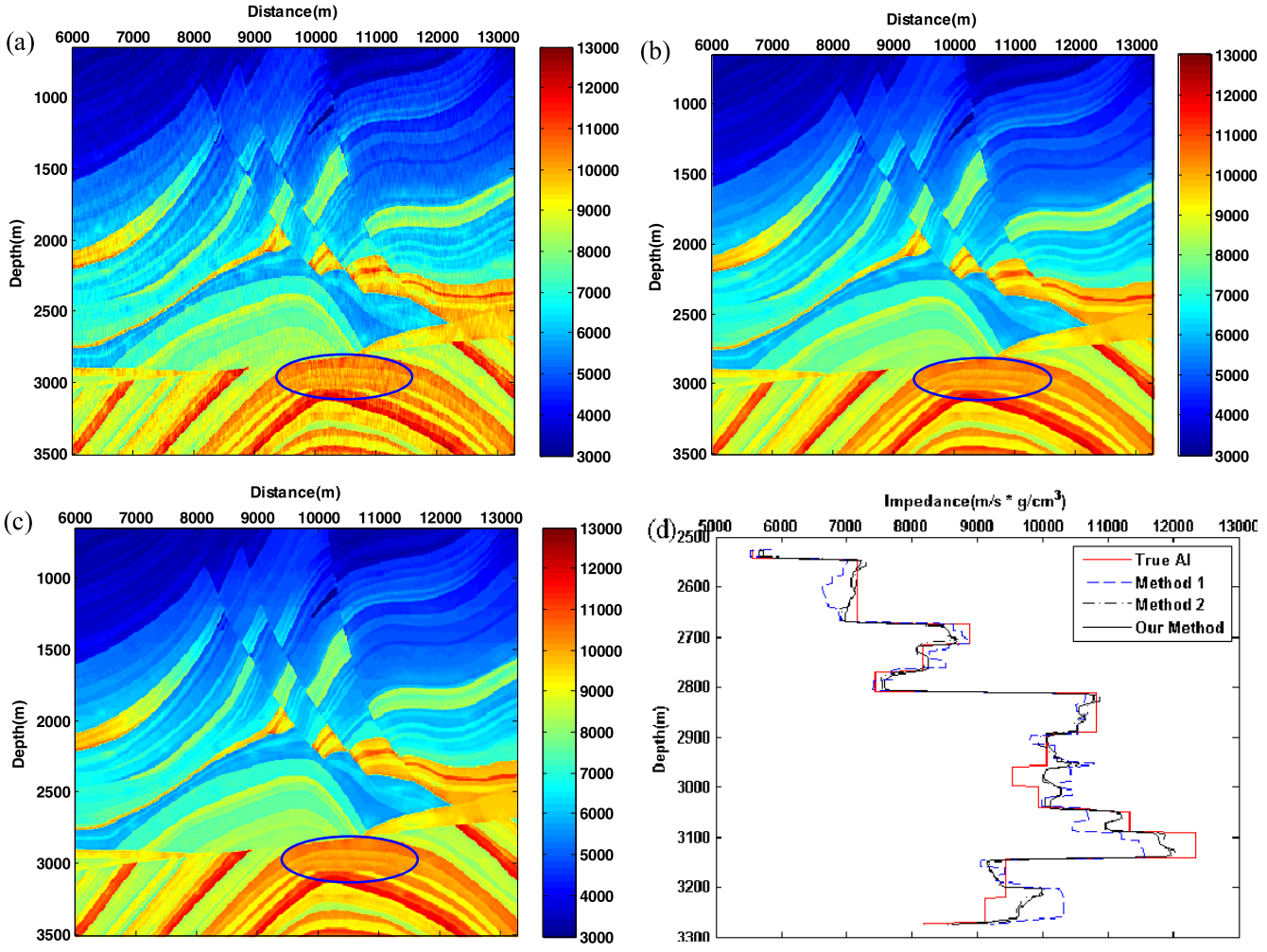

Figure 3. (a) Inversion result of method 1, (b) inversion result of method 2, (c) inversion result of our method and (d) inversion result of a part of the data from trace 1200.

To display the inversion error quantitatively, we calculate the root mean square error (RMSE) of these methods, which is shown in table 1. It can be seen that the RMSE of our method is the smallest. The RMSE of method 2 is slightly larger than that of our method, and the RMSE of method 1 is much larger than that of the other two methods.

In order to compare the inversion error of these three methods more clearly, we calculate the absolute error of the

Table 1. RMSE of the inversion result of three kinds of method.

Method	Method 1	Method 2	Our method	Initial AI model
RMSE	405.52	318.56	306.37	723.40
Percentage of the RMSE reduction	43.94%	55.96%	57.65%	/

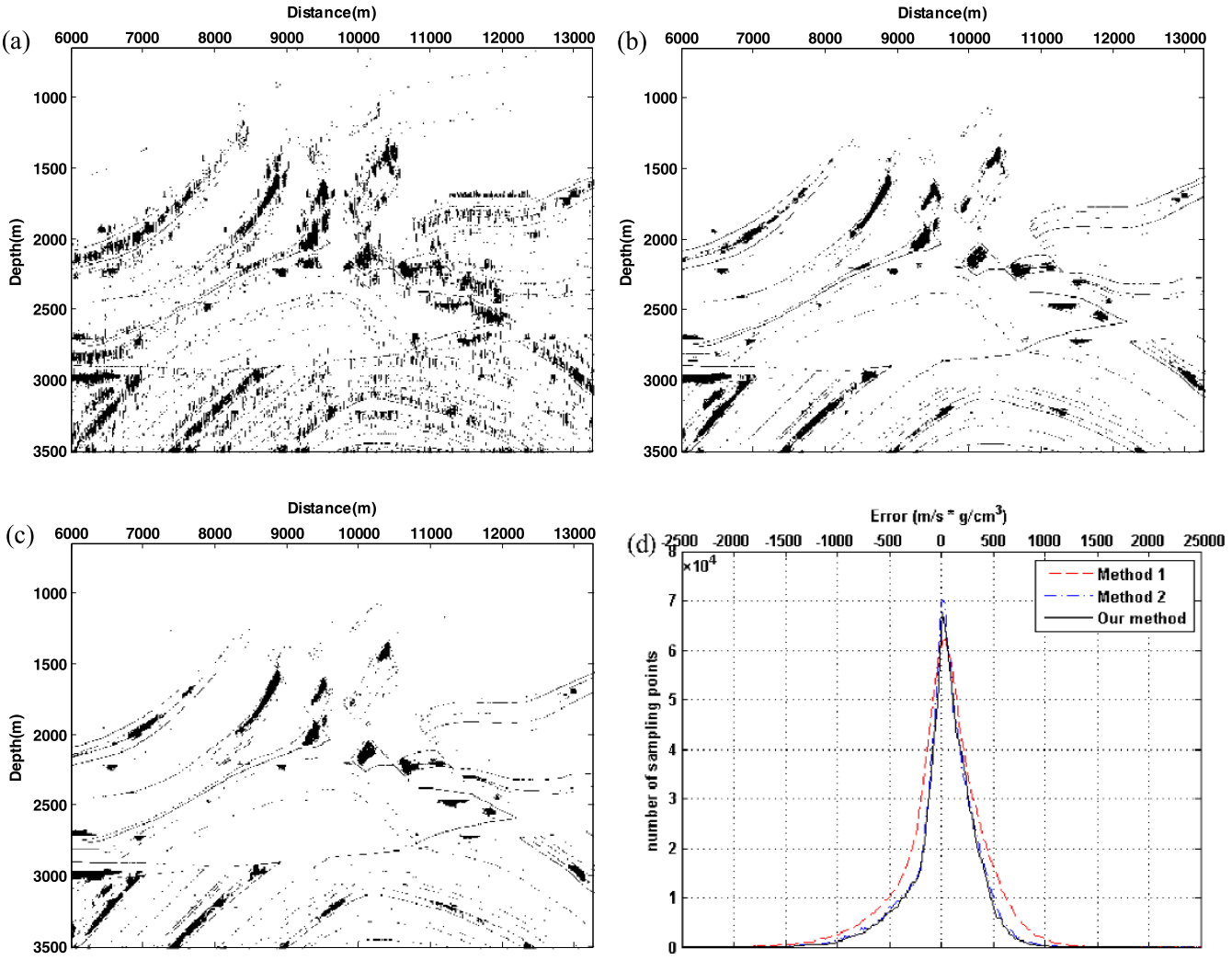

Figure 4. Absolute error graph of the inversion result using method 1 (a), method 2 (b) and our method (c) after binarization processing. (The black point means where absolute error is greater than or equal to 700, otherwise, it is less than 700.) (d) Error distribution of inversion results.

inversion results for these three methods. Then, a binarization processing is performed on the absolute error graph. When the absolute error is greater than or equal to a threshold, its gray value in the error graph is set to 0. Conversely, if the absolute error is less than a threshold, its gray value in the error graph is set to 255. Since the RMSE of the initial AI model in our experiment is 723.40, we simply set the threshold to be 700 (the maximum absolute error of our method is 2517), and the absolute error graphs after binarization processing are shown in figures 4(a)–(c).

From figures 4(a)–(c), we can find that the error of method 1 is distributed in a larger area than that of the other two methods. The error of method 2 and our method are mainly distributed in some blocky areas. Figure 4(b) and (c) are very similar except for the number of black points in figure 4(c) are slightly smaller than that in figure 4(b). Figure 4(d) shows the histogram lines of the inversion error. The red dashed line, blue dash-dotted line and black solid line represent the histogram lines of method 1, method 2 and our method respectively. It can be found that the area surrounded by the red dashed line and the horizontal axis is larger than that of the other two lines, and the red dashed line covers the widest range. This also means the error of method 1 is the largest, and is distributed in a larger area than the other two methods. The histogram lines of our method and method 2 are very similar. If we take a close look at these two lines, we will find that the area surrounded by the histogram line of our method and the horizontal axis is slightly smaller than that of

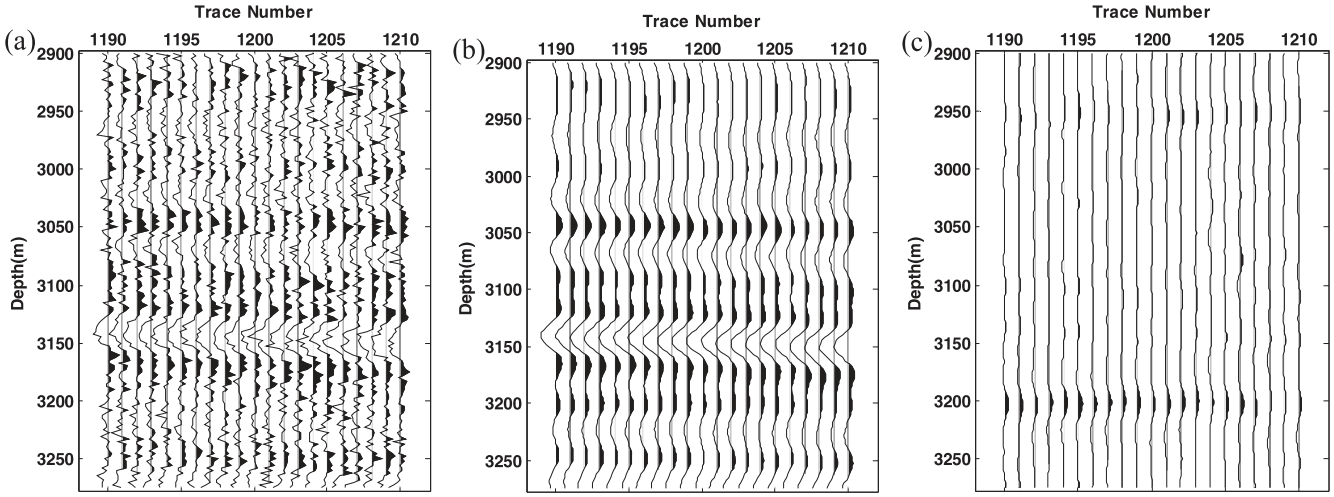

Figure 5. (a) Part of the original noisy synthetic seismic section, (b) part of the seismic section inverted by using our method and (c) the residual error section (obtained by figures 5(b)–1(d)).

the other one. It shows that the error of our method is slightly smaller than that of method 2.

We can see from the above experimental results that since the initial model constrain and multi-trace inversion are used in all these methods, they can all obtain the general situation of the true AI model. Since the L1 norm regularization is used in method 1, the AI inversion result of method 1 has the shape of stair-steps. Because of the influence of noise and lack of TV regularization, the inversion result of method 1 has many errors compared with the other two methods. Moreover, it cannot clearly outline the target reservoir (see figure 3(a)). The inversion results of method 2 and our method are very similar. Both of them have a blocky structure, their errors are relatively small, and they both reveal the target reservoir clearly. Compared with method 1, the advantages of method 2 and our method come mainly from the use of TV regularization. If we take a closer look at the results of method 2 and our method, we find that our method has a slightly smaller error than method 2 (see table 1 and figures 4(b)–(d)). This means that under the condition of TV regularization, adding L1 regularization cannot greatly improve the inversion results. This is due to the fact that TV regularization also has a certain sparsity constraint effect on the inversion result.

Figure 5(a) shows part of the original noisy synthetic seismic section. Figure 5(b) shows part of the inverted seismic section obtained using our method. Comparing it with figure 1(d), we find that they are very similar. The residual error section is the difference between the inverted seismic section and the noise-free synthetic section, which is shown in figure 5(b). It can be seen that the residual error of our method is small.

Figure 6 shows the relationship between the value of each term in objective function (equation (22)) and the iteration number. Note that since each time we invert a block (the size is 140×140) of the seismic section, figure 6 is generated by inverting one of the blocks. For convenience, the first to seventh terms in objective function are denoted by Fidelity term, L1 of reflectivity, TV term, Gamma term, Lambda term1, Lambda term2 and Model constraint term, respectively. Their value vs. the iteration number are shown in figures 6(a)–(g). The value of the objective function vs. the iteration number is shown in figure 6(h).

We can find that the values of the Fidelity term and Objective function have a rapid descent as the iteration number increases, and converge to their optimum value. The initial value of Gamma term, Lambda term1 and Lambda term2 are not equal to 0. With the increase of the iteration number, the value of these three terms increases fast and then rapidly converges to a small value. The initial value of reflectivity $\mathbf{R}$ is 0, thus L1 of reflectivity's value is 0 in the first iteration. Model constraint term's initial value is 0, this is due to the fact that AI's initial value is the initial model's value. Since the initial value of d_x and d_y in algorithm 1 are $\mathbf{0}$, TV term's initial value is 0. With the increase of the iteration number, the value of L1 of reflectivity, Model constraint term and TV term increase first and then converge to their optimum solution. It can be seen from figure 6 that the execution of algorithm 1 is normal.

3.2. Field data

We apply method 1, method 2 and our method to a 2D field data, which is from an oil field in China. The seismic section is shown in figure 7(a), which consists of 200 traces. The sampling interval in time direction is 2 ms. Figure 7(b) shows the initial AI model. The parameters are set as follows: $\mu = 1 \times 10^{-8}$, $\gamma = 5$, $\lambda = 50$, $\alpha = 5$ and $tol = 1 \times 10^{-5}$. Note that method 1 does not use the parameter λ, and method 2 does not use the parameter γ.

The inversion results of method 1, method 2 and our method are shown in figure 8. As can be seen from figures 8(a)–(c), the results obtained by these three methods are similar. However, if we look closely, we will find the result of method 1 has obvious noise and discontinuity. Compared with method 1, method 2 and our method have better lateral continuity and anti-noise ability. Moreover, method 2 and our method have got blocky AI structures.

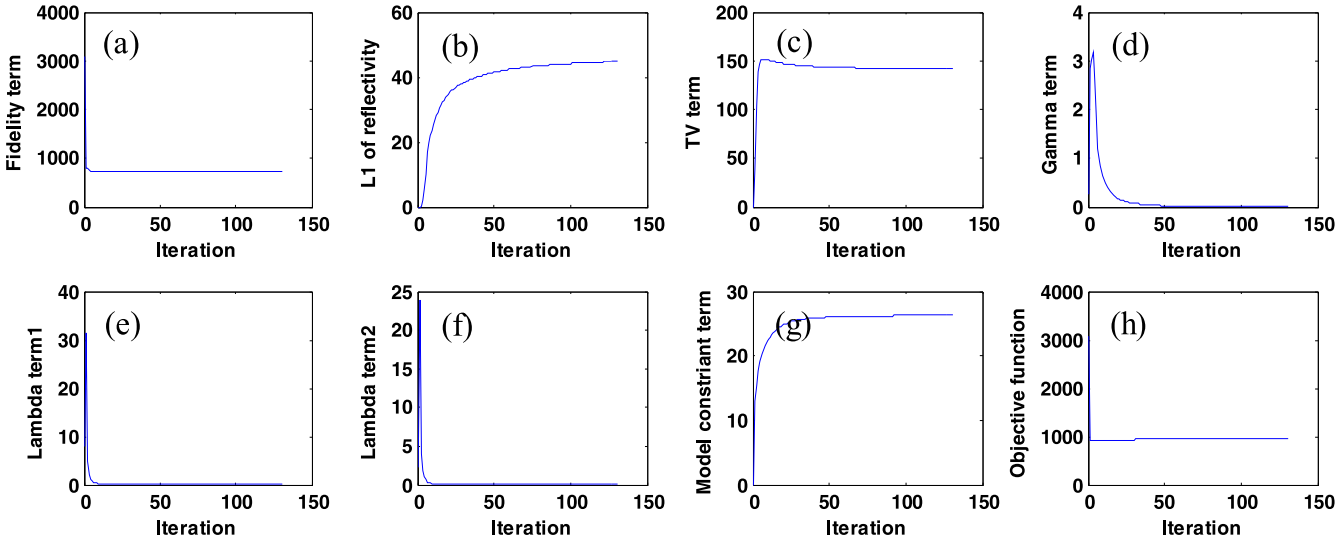

Figure 6. The value of each term in the objective function and the objective function itself versus the iteration number.

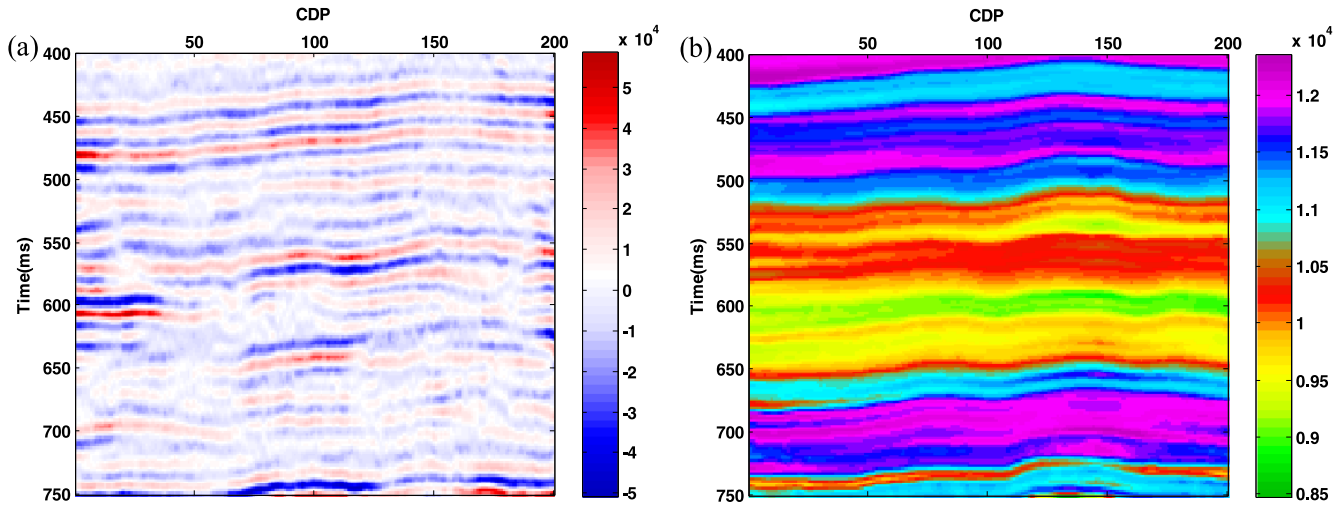

Figure 7. (a) Field seismic data and (b) initial AI model.

There is a well in figure 7, located at CDP166. Figure 8(d) shows the inversion result of method 1, method 2 and our method at CDP166. The red dash-dotted line, black dashed line, blue dashed line, blue solid line and black solid line represent, respectively, the well AI filtered by a Gauss low-pass filter, initial AI model, inversion result of method 1, inversion result of method 2 and inversion result of our method. It can be seen from figure 8(d) that, although all these methods can obtain the general situation of the well AI, our method has less inversion error than the other two methods.

As can be seen from figure 8, by using TV regularization the AI inversion method can have better anti-noise performance and lateral continuity than L1 norm regularization. Using TV regularization and L1 norm regularization, the AI inversion method can obtain a slightly smaller error than using TV regularization alone.

Figure 9 shows part of the field seismic section, inverted seismic section obtained by using our method and residual error section. The residual error section is the difference between the inverted seismic section and the field seismic section. It can be seen that the inverted section is similar to the field section, and the residual error is acceptable.

In order to observe the convergence performance of our method. We show the value of each term in the objective function and the objective function itself vs. the iteration number in figure 10. The meanings of the lines in figure 10 are described in detail in figure 6; we will not repeat them here. Similarly to that shown in figure 6, we can find from figure 10 that the execution of our method is normal in the field data.

4. Conclusions

In this paper, we have analyzed a two-step AI inversion method based on L1 norm regularization. This approach is

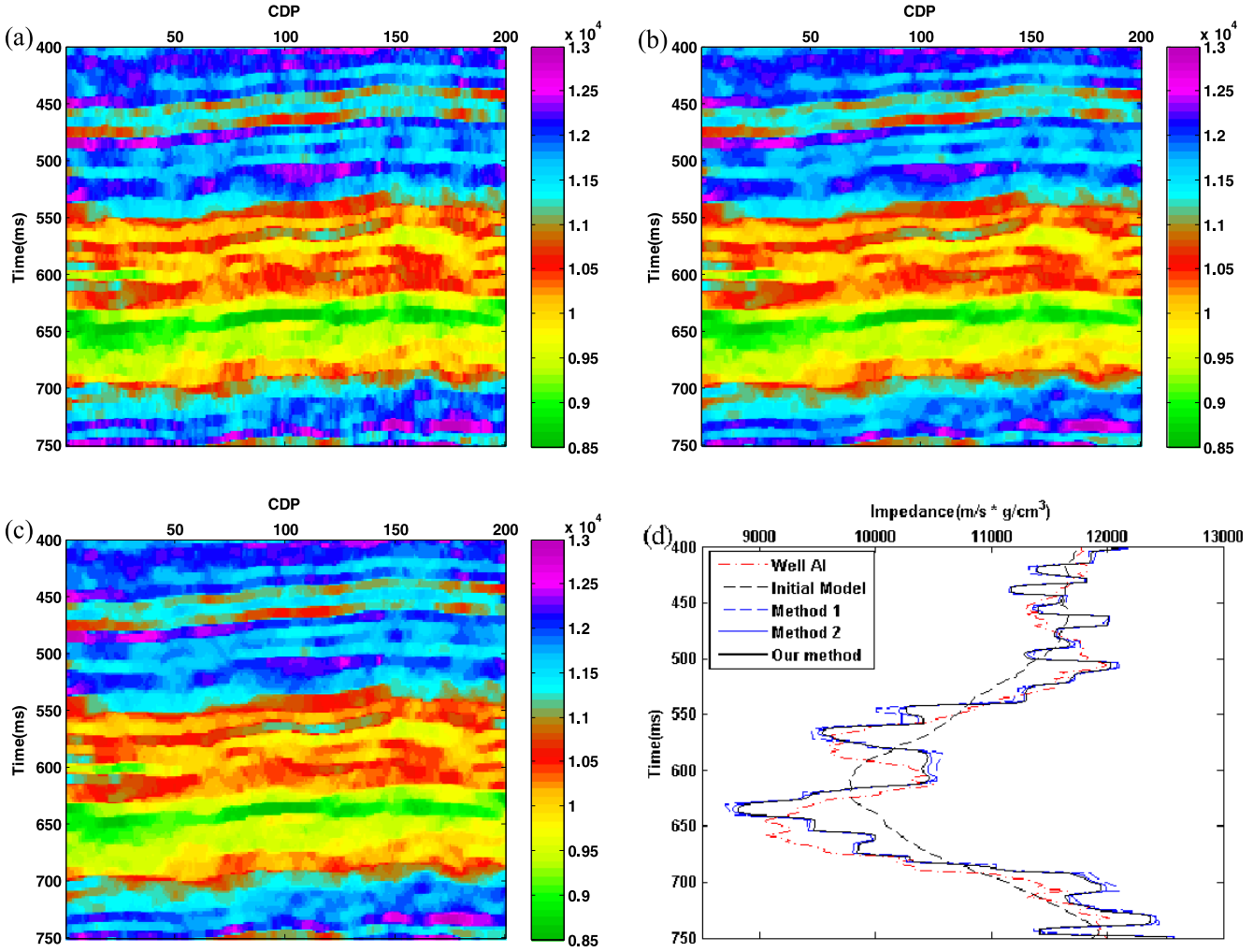

Figure 8. (a) Inversion result obtained by using method 1, (b) inversion result obtained by using method 2, (c) inversion result obtained by using our method and (d) inversion result of the seismic trace at well location (CDP166).

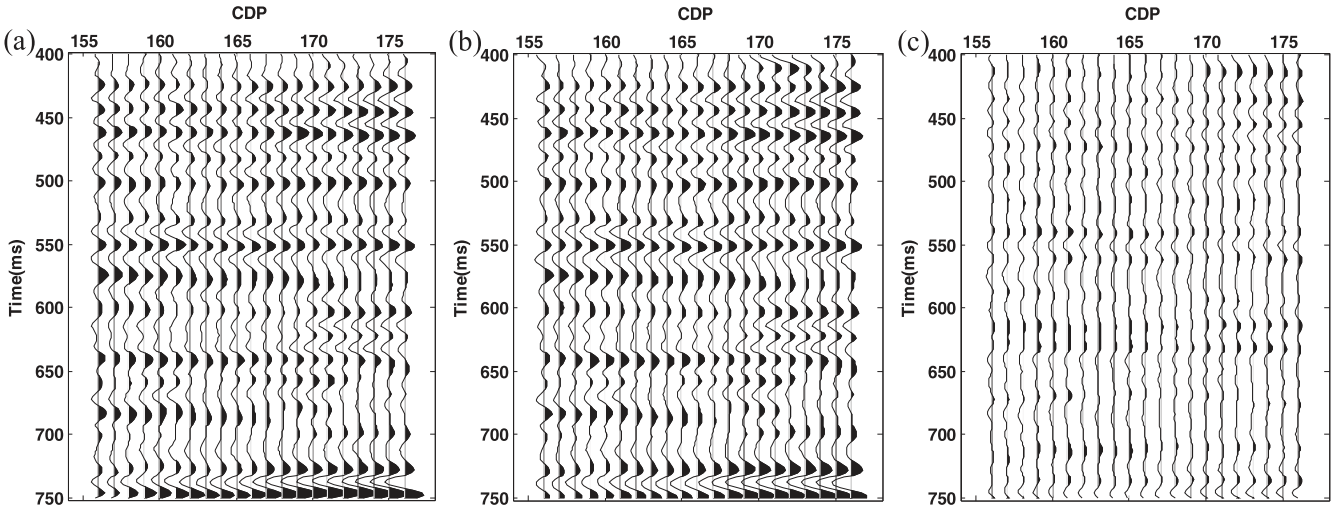

Figure 9. (a) Part of the field seismic section, (b) inverted seismic section obtained by using our method and (c) residual section (obtained by (b)–(a)).

closely related to the AI at time $t = 0$ and the result of reflectivity inversion. If the AI at time $t = 0$ or reflectivity is inaccurate, the inversion result will deviate from the true value. To overcome this problem, we propose an AI inversion method to get AI directly, based on L1 norm regularization, TV regularization, initial model constraint and multi-trace

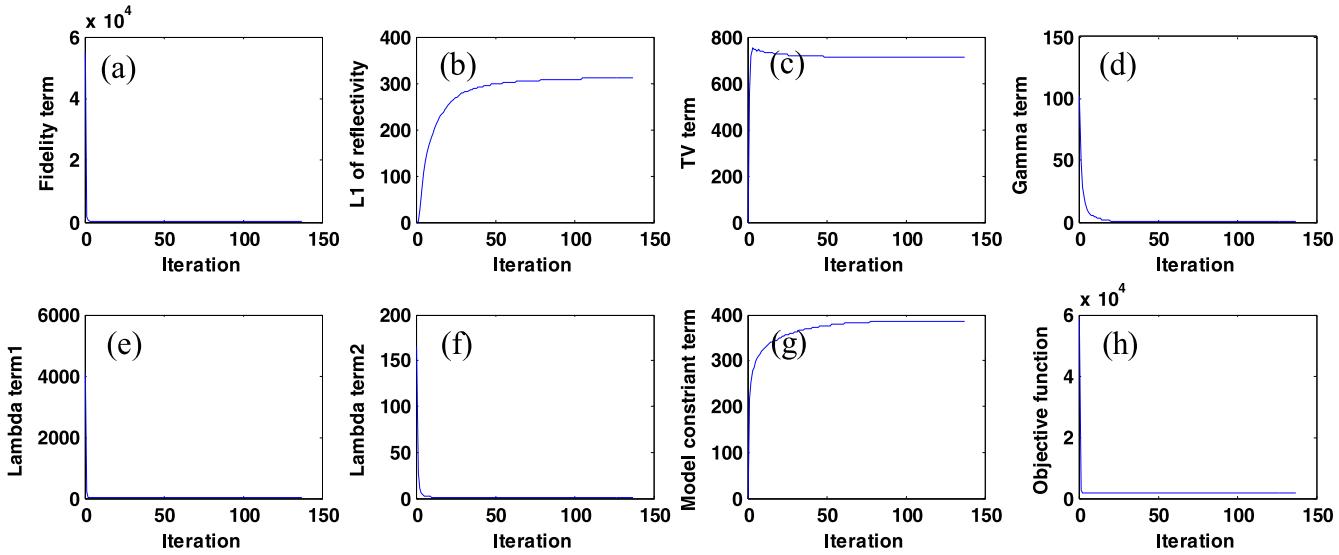

Figure 10. The value of each term in the objective function and the objective function itself versus the iteration number.

inversion. Although these constraints have been separately used in existing AI inversion methods, there is no one method using them together. In our method, the logarithm of AI is the optimization target of the objective function, and the L1 norm sparse constraint is imposed on the reflectivity. To obtain an AI inversion result that better accords with the *a priori* information, we apply all these regularization constraints to our method. However, the multi-regularized method is difficult to calculate. An algorithm based on the split Bregman iteration is developed to solve this problem. We have tested our method and another two methods with Marmous2 model and field data, and compared the results of these three methods. The first method is based on L1 norm regularization, multi-trace inversion and initial model constraint. The second method is based on TV regularization, multi-trace inversion and initial model constraint.

Our experimental results show that compared with L1 norm regularization, the inversion result obtained by using TV regularization has less error and better lateral continuity. The joint use of TV regularization and L1 norm regularization can obtain a slightly smaller error than using only TV regularization. However, the more regularization terms used, the more regularization parameters are needed. How to effectively set the regularization parameters when using a variety of regularization constraints will be the subject of our future work.

Acknowledgments

This work is supported by the National Natural Science Foundation of China (under grants 61571096, 41301460 and 41274127). The authors thank the anonymous referees for their valuable suggestions, which helped us to improve the quality of this article greatly. The authors also thank Chengdu Jingshi Petroleum Technology Co., Ltd for providing us with the field data.

References

Berteussen K and Ursin B 1983 Approximate computation of the acoustic impedance from seismic data *Geophysics* **48** 1351–8
Bube K P and Langan R T 1997 Hybrid ℓ1/ℓ2 minimization with applications to tomography *Geophysics* **62** 1183–95
Cooke D A and Schneider W A 1983 Generalized linear inversion of reflection seismic data *Geophysics* **48** 665–76
Gholami A 2015 Nonlinear multichannel impedance inversion by total-variation regularization *Geophysics* **80** R217–24
Ghosh S K 2000 Limitations on impedance inversion of band-limited reflection data *Geophysics* **65** 951–7
Goldstein T and Osher S 2009 The split Bregman method for L1-regularized problems *SIAM J. Imag. Sci.* **2** 323–43
Guitton A and Verschuur D J 2004 Adaptive subtraction of multiples using the L1-norm *Geophys. Prospect.* **52** 27–38
Hamid H and Pidlisecky A 2015 Multi-trace impedance inversion with lateral constraints *Geophysics* **80** M101–11
Hao H, Liaw A, Junyu B, Zilong X, Yunfei X and Tianshou X 2014 Nonlinear hybrid optimization algorithm for seismic impedance inversion *Int. Geophysical Conf. & Exposition (Beijing, China, 21–24 April 2014)* (Society of Exploration Geophysicists and Chinese Petroleum Society) pp 541–4
Hendrick N and Hearn S 1993 Evaluation of seismic trace inversion techniques *Explor. Geophys.* **24** 549–60
Kong D and Peng Z 2015 Seismic random noise attenuation using shearlet and total generalized variation *J. Geophys. Eng.* **12** 1024–35
Latimer R B, Davidson R and Riel P 2000 An interpreter's guide to understanding and working with seismic-derived acoustic impedance data *The Leading Edge* **19** 242–56
Levy S and Fullagar P K 1981 Reconstruction of a sparse spike train from a portion of its spectrum and application to high-resolution deconvolution *Geophysics* **46** 1235–43
Lindseth R O 1979 Synthetic sonic logs—a process for stratigraphic interpretation *Geophysics* **44** 3–26
Liu C, Song C, Lu Q, Liu Y, Feng X and Gao Y 2015 Impedance inversion based on L1 norm regularization *J. Appl. Geophys.* **120** 7–13
Loris I, Nolet G, Daubechies I and Dahlen F A 2007 Tomographic inversion using ℓ1-norm regularization of wavelet coefficients *Geophys. J. Int.* **170** 359–70

Mabrouk W M 2010 Acoustic impedance inversion approach from petrophysical data *J. Pet. Sci.* E **73** 181–4
Martin G S, Wiley R and Marfurt K J 2006 Marmousi2: an elastic upgrade for Marmousi *The Leading Edge* **25** 156–66
Oldenburg D W, Scheuer T and Levy S 1983 Recovery of the acoustic impedance from reflection seismograms *Geophysics* **48** 1318–37
Russell B H 1988 *Introduction to Seismic Inversion Methods* (Tulsa, OK: Society of Exploration Geophysicists)
Santosa F and Symes W W 1986 Linear inversion of band-limited reflection seismograms *SIAM J. Sci. Stat. Comput.* **7** 1307–30
Taylor H L, Banks S C and McCoy J F 1979 Deconvolution with the ℓ1 norm *Geophysics* **44** 39–52
Velis D R 2006 Parametric sparse-spike deconvolution and the recovery of the acoustic impedance *SEG Technical Program Expanded Abstracts 2006* pp 2141–5
Velis D R 2008 Stochastic sparse-spike deconvolution *Geophysics* **73** R1–9
Walker C and Ulrych T J 1983 Autoregressive recovery of the acoustic impedance *Geophysics* **48** 1338–50
Wang Y F 2010 Seismic impedance inversion using l(1)-norm regularization and gradient descent methods *J. Inverse Ill-Posed Problems* **18** 823–38
Yilmaz Ö 2001 *Seismic Data Analysis* (Tulsa, OK: Society of Exploration Geophysicists)
Yuan S Y, Wang S X, Luo C M and He Y X 2015 Simultaneous multitrace impedance inversion with transform-domain sparsity promotion *Geophysics* **80** R71–80
Zhang F, Dai R and Liu H 2014 Seismic inversion based on L1-norm misfit function and total variation regularization *J. Appl. Geophys.* **109** 111–8
Zhang R, Sen M K and Srinivasan S 2013 A prestack basis pursuit seismic inversion *Geophysics* **78** R1–11
Zwartjes P and Gisolf A 2007 Fourier reconstruction with sparse inversion *Geophys. Prospect.* **55** 199–221